

Efficiency Enhancement of Wide Bandgap Lead Perovskite Solar Cells with PTAA Surface-Passivated with Monomolecular Layer from the Viewpoint of PTAA Band Bending

Huan Bi,* Jiaqi Liu, Raminta Beresneviute, Daiva Tavgeniene, Zheng Zhang, Liang Wang, Gaurav Kapil, Chao Ding, Shahrir Razey Sahamir, Yoshitaka Sanehira, Ajay Kumar Baranwal, Takeshi Kitamura, Dandan Wang, Yuyao Wei, Yongge Yang, Dong-Won Kang, Saulius Grigalevicius,* Qing Shen,* and Shuzi Hayase*



Cite This: <https://doi.org/10.1021/acsami.3c08655>



Read Online

ACCESS |



Metrics & More



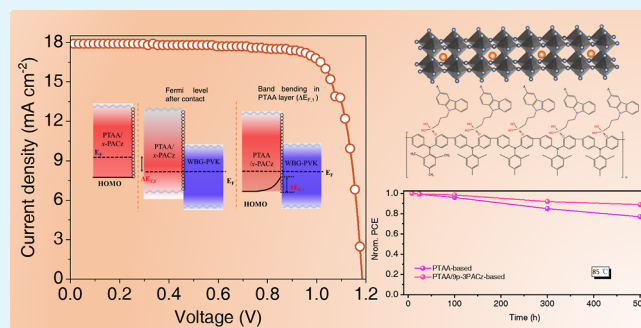
Article Recommendations



Supporting Information

ABSTRACT: This report is on the efficiency enhancement of wide bandgap lead halide perovskite solar cells (WBG Pb-PVK PSCs) consisting of $\text{FA}_{0.8}\text{Cs}_{0.2}\text{PbI}_{1.8}\text{Br}_{1.2}$ as the light-harvesting layer. WBG Pb-PVK PSCs have attracted attention as the top layer of all perovskite-tandem solar cells. Poly[bis(4-phenyl) (2,4,6-trimethylphenyl) amine] (PTAA), a conductive polymer, is always used as the hole transporting layer (HTL) for Pb-PVK PSCs. Nevertheless, the hydrophobic surface of the PTAA sometimes destroys the growth of the $\text{FA}_{0.8}\text{Cs}_{0.2}\text{PbI}_{1.8}\text{Br}_{1.2}$ film. On the other hand, the Fermi level of PTAA is not well matched with that of perovskite film. Thus, the PCE of the WBG Pb-based PSCs with PTAA as the HTL was not very high. In this report, the efficiency of the $\text{FA}_{0.8}\text{Cs}_{0.2}\text{PbI}_{1.8}\text{Br}_{1.2}$ is improved by passivating the surface of the PTAA with a monomolecular layer, where the surface becomes hydrophilic, and the band bending of the PTAA layer is improved to cause swift hole collection. Finally, WBG Pb-PVK PSCs (1.77 eV) with 16.52% efficiency are reported.

KEYWORDS: wide-bandgap perovskite solar cells, phosphonic acid-based molecules, band bending, interface modification, monomolecular



INTRODUCTION

The certified efficiency of single-junction halide perovskite solar cells (PSCs) is now 25.7%,¹ and further research to fabricate Pb-perovskite (PVK) PSCs with large areas or large modules is progressing. To further enhance the efficiency, perovskite tandem cells have attracted interest. Generally, the tandem PSCs comprise the top cell (a wide bandgap (WBG) solar cell) and the bottom cell (a narrow bandgap (NBG) solar cell). Now, the efficiency of Pb-PVK PSCs(top)/Si solar cells (bottom), Pb-PVK PSCs(top)/CIGS solar cells(bottom), and all perovskite tandem solar cells (Pb PSCs(top)/Sn/Pb alloyed PVK PSCs (bottom)) is now 32.5, 24.2, and 29.0%,^{1–4} respectively. The top Pb-PVK PSCs with a bandgap of 1.5–1.65 eV have been coupled with the bottom cell of Si solar cells with a bandgap of 1.1–1.2 eV. According to the results of simulation and experiment, the top Pb-PVK PSCs with a WBG of 1.7–1.8 eV are needed for the all-perovskite tandem solar cells because the bottom cell of Sn/Pb alloyed PVK PSCs has a bandgap of 1.25–1.30 eV.^{5–7} $\text{FA}_{0.8}\text{Cs}_{0.2}\text{PbI}_{1.8}\text{Br}_{1.2}$ is commonly employed as the light-harvesting layer of WBG Pb PSCs with inverted structures. The highest efficiency reported so far is 17.72%.⁸ The top Pb-PVK PSCs have the structure of a

transparent conductive layer/hole transport layer (HTL)/Pb PVK (light harvesting layer)/electron transfer layer (ETL)/electrode. Poly[bis(4-phenyl) (2,4,6-trimethylphenyl) amine] (PTAA) have been employed as the HTL in the inverted Pb-PVK PSCs. However, the poor wettability (hydrophobic surface property) is not favorable for the growth of the Pb-PVK PSCs with high quality.^{9,10} Pan et al. modified the surface of PTAA with toluene during the high-speed spin-coating process of dimethylformamide and improved the wettability. Since the morphology of the Pb-PVK ((FAPbI₃)_{0.85}(MAPbBr₃)_{0.15}) fabricated on the PTAA layer and the contact between the PTAA and Pb-PVK layer was improved, they have reported 19.13% efficiency.¹¹ As a similar approach, Huang et al. improved the wettability of PTAA by pre-spin-

Received: June 15, 2023

Accepted: August 10, 2023

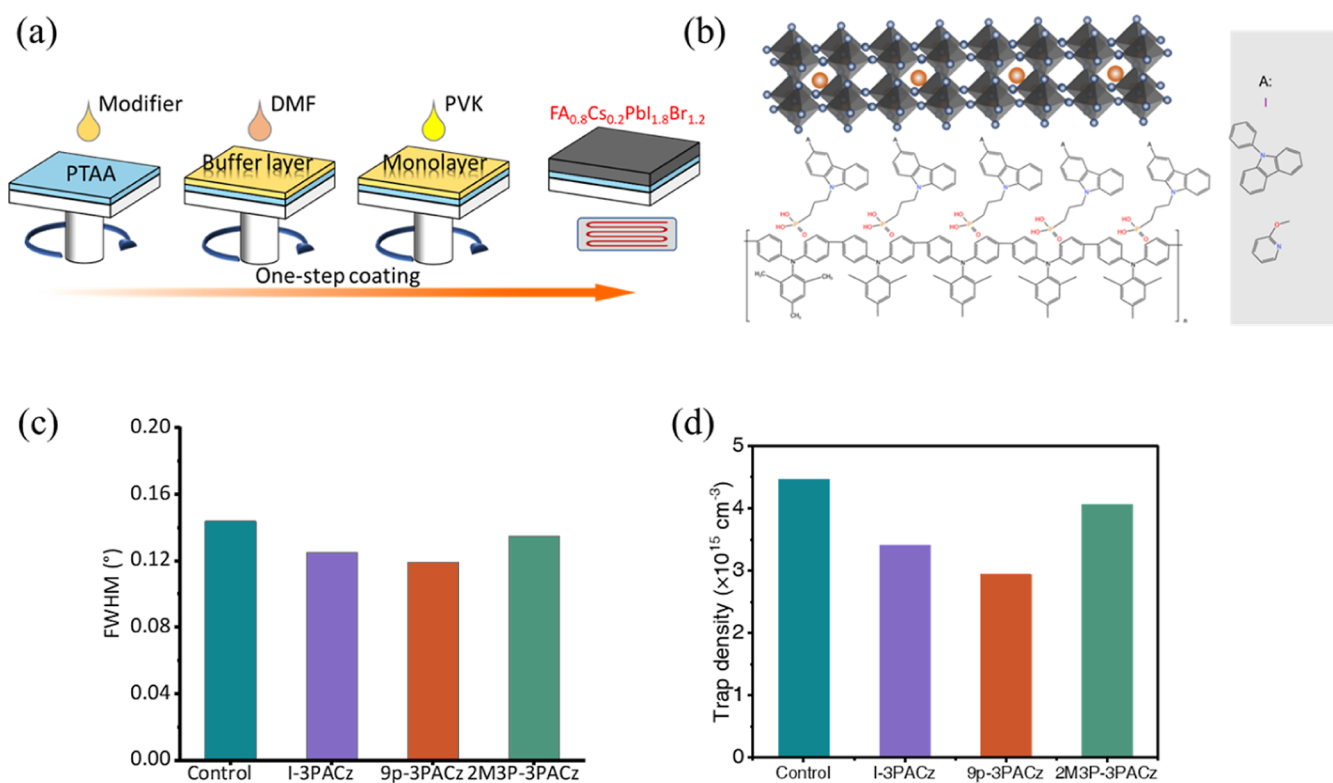


Figure 1. (a) Preparation of PTAA/monomolecular layer/WBG PVK layer. (b) Schematically illustrated PTAA/monomolecular layer/WBG PVK layer, (c) full width at half maximum (fwhm) of X-ray diffraction (XRD) peak at 14.75° assigned to (100) of perovskite layer prepared on the PTAA with and without monolayer. (d) Trap density of PVK layer fabricated on PTAA with and without monolayer, estimated by SCLC method with the hole-only device with the structure of ITO/PTAA/*x*-3PACz(monolayer)/PVK/Spiro-OMeTAD/Ag.

coating a mixed solution of DMF and DMSO on the PTAA.¹² Chen and his group inserted poly[(9,9-bis(3'-(*N,N*-dimethylamino)propyl)-2,7-fluorene)-alt-2,7-(9,9-dioctylfluorene)] (PFN) thin layer between the PTAA layer and Pb-PVK layer. The quality of the Pb-PVK films grown on the PFN layer was improved due to the improved surface wettability. They reported 12.78% efficiency of PEA₂MA_{3.5}FA_{0.5}Pb₅I₁₆ PVK PSCs.¹³

In addition, the energy matching of the conduction band, the valence band, and the Fermi level among HTL and Pb-PVK is necessary for enhancing the efficiency of the Pb-PVK PSCs. So far, many strategies have been proposed to improve the energy level alignment in devices, such as additive engineering and interface engineering.^{14–17} Wu et al. introduced potassium fluoride (KF) at the PTAA and Pb-PVK layers interface. They have reported that the KF treatment improved the energy level arrangement, and the hole extraction efficiency was significantly improved. They reported 21.51% efficiency of Cs_{0.05}(FA_{0.88}MA_{0.12})_{0.95}PbI₃ PSCs.¹⁸ Wang et al. inserted poly(methyl methacrylate) (PMMA) between the PTAA and MAPbI₃. The results showed that the PMMA thin layer adjusted the interface energy level and facilitated charge carrier transfer. The efficiency of the MAPbI₃ PSCs was improved from 17.39 to 19.51%.¹⁹ In these surface modifications, thin-layer polymer films have been used. Fabrication of thin polymer films is complex, and the film thickness drastically affects solar cell performances.²⁰

Self-assembled monomolecular layers have proven useful as the HTL for high-efficiency Pb-PVK PSCs.^{21–23} The monolayer molecules used for the HTL contain p-type, linker,

and anchor groups. Among them, molecules with phosphonic acids as the anchor group, such as (*x*-(9H-carbazol-9-yl)propyl)phosphonic acid (*x*PACz, where *x* stands the alkyl chain length), are commonly employed in PSCs. For example, Tan and his coauthor used the carbazole group as the p-type group and phosphonic acid as HTL to improve the PCE of the tandem solar cell and have reported 24.7% in tandem solar cells.²⁴ Our groups have reported an efficiency of over 23% of Sn/Pb alloyed PSCs consisting of 2-(9H-carbazol-9-yl) ethyl] phosphonic acid (2PACz) as the HTL.²⁵ The advantage of the monomolecular layer of HTL over the thin polymer layer is that thickness control is easy. Since the surface of the treated substrate was washed away with solvents, unreacted molecules were removed, and molecules bonding to the substrate by the anchor group remained. This result prompted us to passivate the surface of PTAA with a monomolecular layer. Since the PTAA has an N atom showing basic properties and phosphonic acid in the PACz is acid, the surface of the PTAA is passivated with only mono molecular layers after the treated surface is washed with solvents.^{26–28} We now report the PTAA layer surface-passivated with 3PACz with various p-type groups. The energy level change (balance band and Fermi level) of PTAA and the surface energy change of the PTAA by the mono-molecular layer passivation are discussed.

RESULTS AND DISCUSSION

In order to improve the surface properties of PTAA, the surface was passivated with a monomolecular layer of 3PACz consisting of carbazole groups working as p-type properties. The following *x*-3PACz (*x* = 1, 9p and 2M3P) were synthesized: [3-(3-iodocarbazol-9-yl) propyl]phosphonic acid

(I-3PACz), (3-(3-[4-(carbazol-9-yl)phenyl]carbazol-9-yl)propyl) phosphonic acid (9p-3PACz), and (3-[3-(2-methoxy-pyridin-3-yl)carbazol-9-yl]propyl) phosphonic acid (2M3P-3PACz). Figure 1a shows the process of this work. After the PTAA layer was prepared on the indium tin oxide (ITO) substrate, the *x*-3PACz solution was coated. Then, the surface was washed with DMF to remove the *x*-3PACz molecules not bonded to the PTAA, followed by spin-coating the perovskite solution.^{25,29} Figure 1b shows the expected layered structure of the PTAA/*x*-3PACz/PVK layer, where the *x*-3PACz monolayer is inserted between the PTAA and the PVK layer. The synthetic route of *x*-3PACz is shown in the experimental section and Scheme S1. Fourier-transform infrared (FTIR) and X-ray photoelectron spectroscopy (XPS) were used to uncover the chemical interaction between PTAA and monolayer molecules. As shown in Figure S1a–c, the peak located on 803 cm⁻¹ is attributed to the vibrations of the P–O bond.³⁰ After being deposited on PTAA, the peak position was shifted to a high wavenumber compared with the bare monolayer molecules. FTIR results suggest a strong chemical interaction exists between PTAA and monolayer. In addition, the N 1s and P 2p XPS peaks of PTAA and PTAA/9p-3PACz were detected by XPS in order further to reveal the chemical interaction between PTAA and 9p-3PACz. As shown in Figure S1d,e, for N 1s, compared with the PTAA film, the PTAA/9p-3PACz has a lower binding energy. While for the P 2p, the PTAA/9p-3PACz shows a higher binding energy compared with the bare PTAA, which indicated that the molecular clouds of N and P were transferred after 9p-3PACz was deposited on PTAA, and this indicated a strong chemical interaction between N (PTAA) and P (9p-3PACz), also consistent with previous reports.³⁰

As shown in Figure S2, the contact angle of the perovskite solution on the substrate was decreased from 79° (PTAA) to 60° (PTAA/I-3PACz), 48° (PTAA/9p-3PACz), and 61° (PTAA/2M3P-3PACz), respectively. The smaller contact angle indicates that the precursor solution is easier to spread on the substrate, which helps to improve the quality of the perovskite film.³¹ Scanning electron microscopy (SEM) images show that the perovskite film morphology was improved (Figure S3). After perovskite film is deposited on PTAA/monolayer, the perovskite film morphology is improved. Figure S4a, b shows the grazing incidence X-ray diffraction (GIXRD) pattern of the perovskite deposited on the different substrates. By changing the X-ray incident angle from small to large, the crystal structure information of the perovskite film from the shallow layer to the deep layer is obtained (Figure S4 a and b). The perovskite thin film on PTAA and that prepared on monolayer passivated PTAA had similar diffraction peak positions at around 14.75, 20.73, and 32.74°, corresponding to (100), (101), and (211) crystal planes of WBG perovskite phase, respectively, suggesting that the surface passivation monolayer on PTAA did not change the perovskite crystal phase and facet from the top to the deeper portion.^{32–34} As shown in Figure S4c, the perovskite film deposited on PTAA/9p-3PACz had narrower FWHM, indicating that the monolayer on PTAA is beneficial to make the crystal size of the perovskite larger. As shown in Figure 1c, the value of full width at half maxima (FWHM) of the perovskite layer deposited on PTAA/9p-3PACz (0.119°) is narrower compared with the one deposited on PTAA (0.143°), indicating that the perovskite film crystal size increased slightly.^{25,29} Finally, we noticed that the diffraction peak intensity of the

perovskite film prepared on PTAA/9p-3PACz was larger than that of the perovskite film on the PTAA only, suggesting that the crystallinity was enhanced on the PTAA/9p-3PACz.

The bandgaps of these perovskite layers were calculated from these UV–vis spectra, as shown in Figure S5. The perovskite prepared on the PTAA layer and surface passivated PTAA gave the same bandgap ($E_g = 1.77$ eV). Meanwhile, as shown in Figure S6, the Urbach energy of the perovskite layer decreased from 60.7 meV (PTAA) to 47.9 meV (PTAA/I-3PACz), 42.2 meV (PTAA/9p-3PACz), and 50.2 meV (PTAA/2M3P-3PACz), respectively, after the surface of PTAA layer was passivated with the monomolecular layer. The small Urbach energy corresponds to the low defect density near the conduction and valence band levels.²⁵ Space charge limited current (SCLC) was measured to evaluate the defect densities of the perovskite films. Figure 1d shows the dark current–voltage (I – V) curves of the hole-only devices with the structure of ITO/PTAA/without or with monomolecular layer (*x*-3PACz)/perovskite/Spiro-OMeTAD/Ag. The defect density was obtained from the following equation^{35,36}

$$n_t = \frac{2\epsilon\epsilon_0 V_{TFL}}{eL^2} \quad (1)$$

where ϵ_0 is the vacuum dielectric constant, ϵ is the dielectric constant of the perovskite, e is the elementary charge, and L is the film thickness of the perovskite. The defect density of the perovskite film deposited on PTAA was 8.58×10^{15} cm⁻³, while that of the perovskite film deposited on PTAA/I-3PACz, PTAA/9p-3PACz, and PTAA/2M3P-3PACz was 4.84×10^{15} cm⁻³, 4.59×10^{15} cm⁻³, and 6.24×10^{15} cm⁻³, respectively. Figure S8 and Figure S9 show the photoluminescence (PL) and time-resolved PL (TRPL) results of the perovskite layer fabricated on the glass/monomolecular/PVK layer. On the monomolecular layer, the PL intensity of the perovskite was enhanced in the following order: 2M3P-3PACz < I-3PACz < 9p-3PACz. The results indicate that the defect of the perovskite decreased in the following order of 9p-3PACz < I-3PACz < 2M3P-3PACz. In addition, TRPL curves were well fitted by the following equation

$$I(t) = A_1 e^{(-t/\tau_1)} + A_2 e^{(-t/\tau_2)} \quad (2)$$

where τ_1 represents the fast decay time, and τ_2 stands for the slow decay time. Additionally, A_1 and A_2 denote the amplitudes of the fast and slow decay processes. The average carrier lifetime (τ_{ave}) was obtained by the equation of^{37,38}

$$\tau_{ave} = \frac{A_1 \tau_1^2 + A_2 \tau_2^2}{A_1 \tau_1 + A_2 \tau_2} \quad (3)$$

these corresponding fitting parameters are presented in Table S1. The carrier lifetime of the perovskite film increased in the following order: 2M3P-3PACz/PVK: 99.13 ns, I-3PACz/PVK: 119.50 ns, 9p-3PACz/PVK: 128.62 ns), which is the order of low defect density and be consistent to the results of SCLC and Urbach energy measurements.

Photoelectron yield spectroscopy (PYS) and Kelvin probe measurement were conducted to investigate the change in the valence band and Fermi energy levels of the device before and after monomolecular passivation. Figure S10 shows the HOMO energy level, the LUMO energy level, and the Fermi energy level of the PTAA with and without monomolecular passivation. The Fermi and valence band energy levels of the PTAA became deeper after the PTAA surface was passivated

with the monomolecular layer. According to previous reports, the direction and strength of the surface dipole affect the vacuum level.^{39,40} These changes in the energy level may be explained by the vacuum level change after the surface passivation, as shown in Figure S11.

Figure 2a shows the band bending in the PTAA layer with or without monolayer modification, calculated from the difference

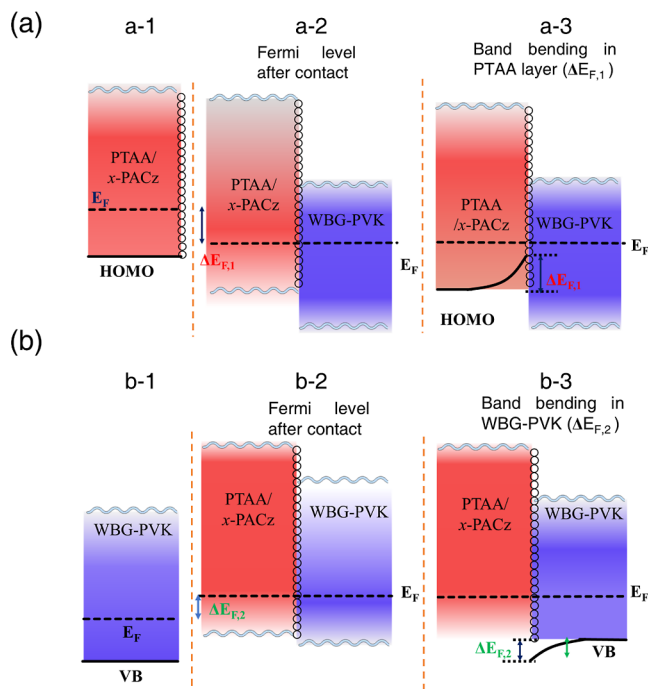


Figure 2. (a) (a-1) Fermi level of PTAA or PTAA/*x*-PACz, (a-2) Fermi level change after contact with WBG-PVK and (a-3) band bending after PTAA or PTAA/*x*-PACz contact with WBG-PVK ($\Delta E_{F,1}$), (b) (b-1) Fermi level of WBG-PVK only, (b-2) Fermi level change after contact with PTAA or PTAA/*x*-PACz and (b-3) band bending after WBG-PVK contact with PTAA or PTAA/*x*-PACz ($\Delta E_{F,2}$). Circles represent *x*-PACz monolayer molecules.

of the Fermi level of the PTAA layer after the perovskite layer was contacted with the PVK. First, we analyzed the band bending of the PTAA and perovskite after contacting each other. The Fermi level of the PTAA was -4.98 eV (Figure 2a(1)). The Fermi level of the PTAA was shifted to -5.4 eV after the PVK was contacted with PTAA (Figure 2a(2)). The Fermi level of the PTAA layer in Figure 2a(2) is the same as that of the PTAA/PVK layer (Figure 2a(2)). The difference between the Fermi level of PTAA before and after the PVK contact was 0.42 eV ($5.4 - 4.98$ eV = 0.42 eV), as shown in Figure 2a(2). Since the HOMO of the PTAA is pinned at -5.17 eV, 0.42 eV band bending is expected, as shown in Figure 2a(3). The band bending becomes a barrier for the hole injection. In the same way, the band bending in the PVK layer was estimated as follows. The Fermi level of the PVK was -5.63 eV (Figure 2b(1)). The Fermi level was changed to -5.4 eV when the PVK contacted the PTAA layer (Figure 2b(2)). The difference in the Fermi level of the PVK before and after the PTAA layer was 0.23 eV ($5.63 - 5.4$ eV = 0.23 eV; Figure 2b(2)). Since the valence band has been pinned at -6.00 eV at the interface, 0.23 eV band bending is expected (Figure 2b(3)). The 0.23 eV becomes a barrier for the hole injection from the PVK layer to the PTAA. It has been reported that the

0.23 eV barrier is not so serious in the previous paper, where the structure is called the spike band structure.^{29,41–43}

The conduction band and the valence band of PTAA were varied after the surface of the PTAA was passivated with various monomolecular layers (Table 1). The band bending of

Table 1. Band Bending ($\Delta E_{F,1}$) of PTAA/*x*-PACz after Contact with WBG-PVK

passivation	only PTAA	I-3PACz	9p-3PACz	2M3P-3PACz
$\Delta E_{F,1}$ (eV)	0.42	0.33	0.25	0.31

the PVK layer was not varied, depending on the interface passivation (Table 2). The band bending of the PTAA layer

Table 2. Band Bending ($\Delta E_{F,2}$) of WBG-PVK after Contact with PTAA/*x*-PACz

passivation	only PTAA	I-3PACz	9p-3PACz	2M3P-3PACz
$\Delta E_{F,2}$ (eV)	0.23	0.23	0.23	0.23

became smaller in the following order: I-3PACz > 9p-3PACz > 2M3P-3PACz. According to the band bending shown in Figure 2, Tables 1 and 2, holes should be accumulated at the interface. Therefore, small-band bending should give higher efficiency, which will be discussed later. In addition, this kind of band change is known to be due to the vacuum level change caused by the dipole moment of the passivation molecules, as shown in Figure S11. Fermi level of the PTAA layer passivated with I-3PACz, 9p-3PACz, 2M3P-3PACz was as follows: $E_{F,I-3PACz} = -5.07$ eV; $E_{F,9p-3PACz} = -5.15$ eV; $E_{F,2M3P-3PACz} = -5.09$ eV, respectively. The effect of the dipole seems to become larger in the following order: 9p-3PACz > 2M3P-3PACz > I-3PACz. Calculating the dipole using the model structure of PTAA and the monomolecular layer seems consistent with the above order, as shown in Figure S12.

The photovoltaic performance of the devices with the structure of ITO/PTAA/(with or without monomolecular layer)/WBG-perovskite/guanidine bromide (GuBr)/C60/BCP/Ag is summarized in Figure 3, where these solar cells with PTAA surface passivated with I-3PACz, 9p-3PACz, 2M3P-3PACz, and without passivation are abbreviated as I-3PACz-based PSCs, 9p-3PACz-based PSCs, 2M3P-3PACz-based PSCs, and PTAA-based PSCs, respectively. The efficiency of the device is shown in Figure 3a and Figure S13. Figure 3b and Table S2 show these PSCs' typical *J*–*V* curves and photovoltaic parameters. The efficiency of the PTAA-based PSCs was 14.43%, with an open-circuit voltage (V_{OC}) of 1.127 V, a short circuit current (J_{SC}) of 17.07 mA cm^{-2} , and a fill factor (FF) of 75.04% under standard AM 1.5G illumination. The efficiency of I-3PACz-based PSCs, 9p-3PACz-based PSCs, and 2M3P-3PACz-based PSCs was 15.81% (J_{SC} of 17.96 mA cm^{-2} , a V_{OC} of 1.158 V, and a FF of 76.20%), 16.52% (J_{SC} of 17.88 mA cm^{-2} , a V_{OC} of 1.177 V, and a FF of 78.54%), and 15.84% (J_{SC} of 17.96 mA cm^{-2} , a V_{OC} of 1.163 V, and a FF of 75.87%), respectively. The enhanced efficiency can be attributed to the decrease in the defect density (SCLC, PL), improved morphology (SEM), and matchable energy level (band bending) after 9p-3PACz surface passivation. In addition, the efficiency of the 9p-3PACz-based PSCs was better than the solar cell consisting of the PTAA/2PACz monomolecular layer, where the 2PACz is frequently employed (Table S2). The incident photon to current

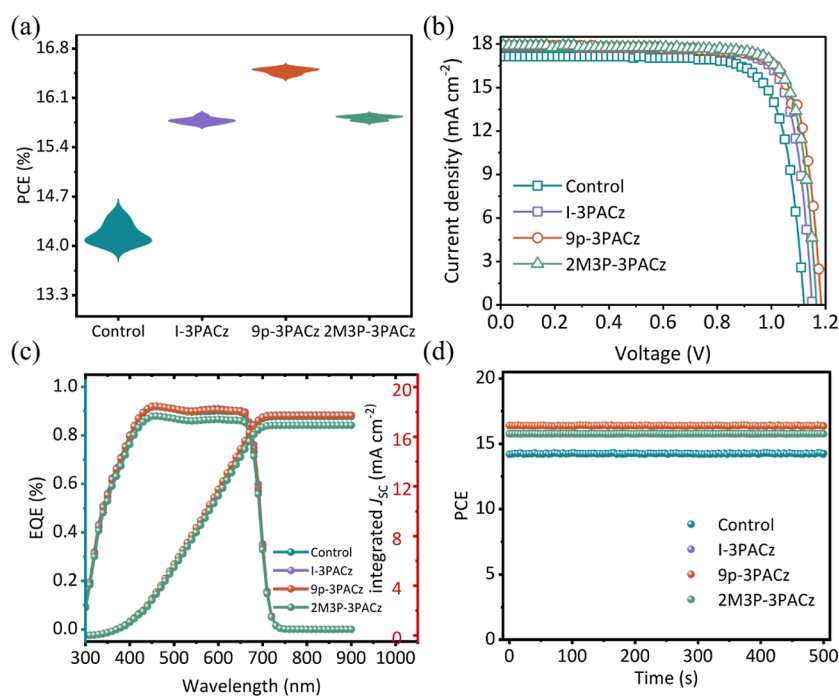


Figure 3. a) Statistical distribution diagram of PCE for the devices (I-3PACz-based PSCs, 9p-3PACz-based PSCs, 2M3P-3PACz-based PSCs, and PTAA-based PSCs). (b) Typical champion $J-V$ curves. (c) IPCE curves of the device. (d) Steady-state current density as a function of time at the maximum power point.

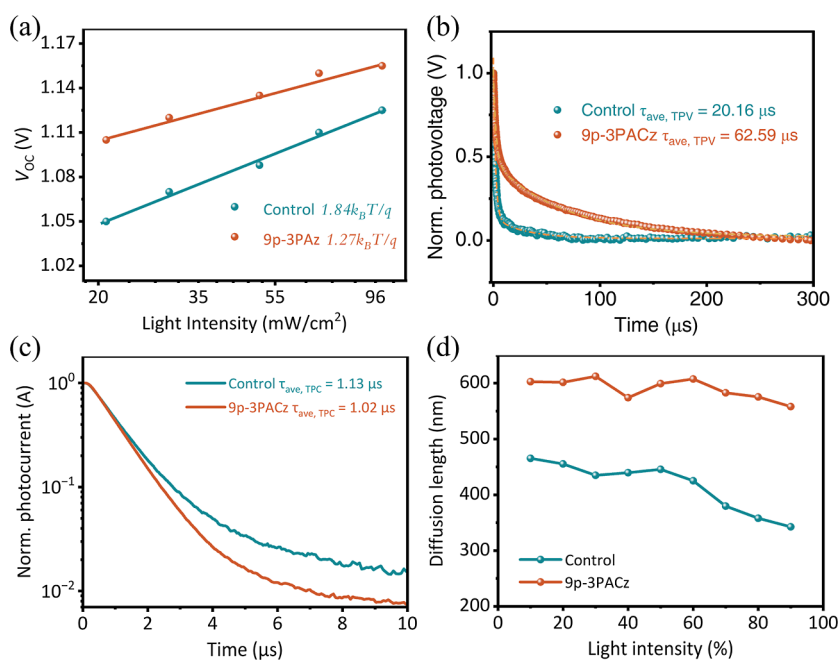


Figure 4. a) V_{OC} versus light intensity of PTAA-based and 9p-3PACz-based PSCs. (b) Transient photovoltage (TPV). (c) TPC curves of PTAA-based PSCs and 9p-3PACz-based PSCs. (d) Diffusion length of PTAA-based PSCs and 9p-3PACz-based PSCs.

conversion efficiency (IPCE) spectra of the PTAA-based PSCs, I-3PACz-based PSCs, 9p-3PACz-based PSCs, and 2M3P-3PACz-based PSCs are presented in Figure 3c. The integrated current density calculated was 16.93 mA cm^{-2} (PTAA-based PSCs), 17.75 mA cm^{-2} (I-3PACz-based PSCs), 17.63 mA cm^{-2} (9p-3PACz-based PSCs), and 17.71 mA cm^{-2} (2M3P-3PACz-based PSCs), respectively, which well matched with those obtained from $J-V$ curves. The maximum power point tracking method measured the relationship between PCE and

irradiation time (Figure 3d). The output was stable during the illumination, and the efficiency after 500 s was 15.75% (I-3PACz-based PSCs), 16.36% (9p-3PACz-based PSCs), and 15.76% (2M3P-3PACz-based PSCs), respectively.

The ideality factor (n) was measured to evaluate the nonradiative recombination of the device. The n closer to 1 shows less nonradiative recombination.⁴⁴ The n can be calculated by the equation of $V_{OC} = (nk_B T/q) \ln(I) + B$,⁴⁴ where k_B , T , and q are the Boltzmann's constant, Kelvin

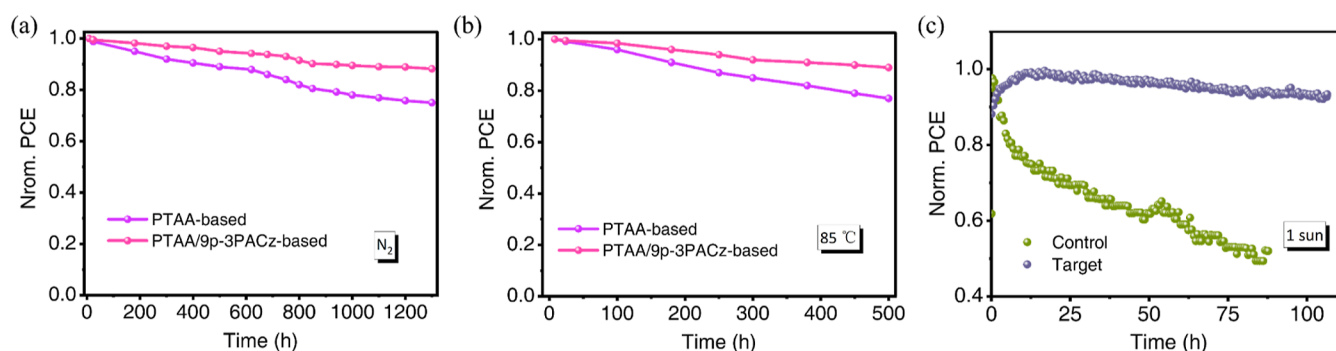


Figure 5. Unencapsulated PSCs stability of the ITO/PTAA/(9p-3PACz)/WBG PVK/C60/BCP/Ag in (a) N_2 atmosphere, (b) hot plate ($85\text{ }^\circ\text{C}$), and (c) 1 sun illumination.

temperature, and element charge, respectively. As shown in Figure 4a, the ideality factor was $n = 1.84$ (PTAA-based PSCs) and $n = 1.27$ (9p-3PACz-based PSCs). This result suggests that the nonradiative recombination of the latter was reduced. The voltage decay time measured by the TPV method was 20.16 ns (PTAA-based PSCs) and 62.59 ns (9p-3PACz-based PSCs).⁴⁵ The carrier recombination resistance (R_{rec}) measured by electrochemical impedance spectroscopy (EIS) at 0 V in the dark is summarized in Figures S14 and S15. A typical semicircular curve was observed. The curve obtains the carrier recombination resistance (R_{rec}). As presented in Figure S15, the R_{rec} of 9p-3PACz-based PSCs was higher than that of PTAA-based PSCs. These results support the explanation that the charge recombination of 9p-3PACz PV is more retarded, compared to that of PTAA PV, which gives higher V_{oc} and FF.^{46,47} Figure S16 shows the PL and TRPL test with ITO/PTAA/(9p-3PACz)/PVK structure. Lower PL peak intensity can be evident for the PL test after 9p-3PACz is introduced. In addition, the TRPL test (Figure S15b and Table S3) shows the less carrier lifetime of the PVK deposited on ITO/PTAA/9p-3PACz (8.91 ns) than perovskite deposited on ITO/PTAA (15.69 ns), which suggested that the 9p-3PACz is suitable for carrier transport. Furthermore, we evaluated the effect of 9p-3PACz on the conductivity of PTAA films. As shown in Figure S17, the conductivity of the PTAA was increased after conductivity 9p-3PACz was deposited on PTAA, which also facilitates the transport of charge carriers.⁴⁸ Transient photocurrent (TPC) was also carried out to uncover the carrier transport with the structure of ITO/PTAA/(9p-3PACz)/perovskite/GuBr/C60/BCP/Ag ((9p-3PACz-based PSCs) and ITO/PTAA/perovskite/GuBr/C60/BCP/Ag ((PTAA-based PSCs). As shown in Figure 4c, the photocurrent decay times reduced from 1.13 μs (the former) to 1.02 μs (the latter). TPV and TRPL result shows that carrier extraction was promoted after the PTAA was passivated with 9p-3PACz. As shown in Figure S18, the built-in potential (V_{bi}) of 9p-3PACz-based PSCs and PTAA-based PSCs obtained by Mott–Schottky curves was 1110 mV and 940 mV, respectively. The enhanced V_{bi} helps to promote charge transfer and transport.^{49,50} The following equation also calculated carrier diffusion length: $L_{\text{D}} = \sqrt{D\tau_{\text{rec}}}$,⁵¹ where D is the diffusion constant of the carriers and τ_{rec} is the electron recombination lifetime.⁵² As shown in Figure 4d, 9p-3PACz-based PSCs had longer carrier diffusion lengths than PTAA-based PSCs. These results strongly support that improved carrier transport and extraction contribute significantly to efficiency improvement.

Unsealed 9p-3PACz-based PSCs and PTAA-based PSCs were stored in the glove box filled with N_2 , and their stability results are summarized in Figure 5. The 9p-3PACz-based PSCs kept 88.2% of the initial efficiency after 1300 h of aging, while the PCE of the PTAA-based PSCs was 75.1% (Figure 5a). In addition, we investigated the thermal stability by holding the device on the hot stage at the temperature of $85\text{ }^\circ\text{C}$ in the glove box. As exhibited in Figure 5b, after aging 500 h, the PTAA-based PSCs retained 77.1% of their original efficiency, while the 9p-3PACz-based PSCs kept 89.2% of their original PCE. It is well known that light can accelerate the phase separation of perovskite films, so to evaluate the effect of 9p-3PACz on the phase separation of perovskite films,^{53–55} we tested the photostability of the devices and the unencapsulated device was placed under continuous sunlight. As shown in Figure 5c, the results show that for the control device, after 87 h, the PCE of the PSCs retained 51% of their original efficiency, while the 9p-3PACz-based PSCs kept 93% of their original PCE after 100 h.

CONCLUSIONS

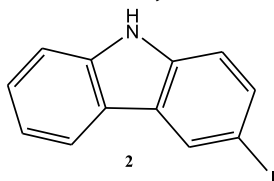
We have synthesized a series of 3PACz-based molecules with different functional groups (1-3PACz, 9p-3PACz, and 2M3P-3PACz) to modify the interface between PTAA and the perovskite film. The PVK with surface passivated PTAA gave improved efficiency. Among them, 9p-3PACz gave the best results. The results were explained by improved PVK layer morphology, less defective PVK film, longer carrier lifetime, longer carrier diffusion length, and swift carrier collection, which were determined by PL, PL decay, V_{oc} decay curve, J_{sc} decay curve, Mott–Schottky plot, and built-in potential. The improved band bending at the surface of PTAA/PVK after the interface was passivated with a monomolecular layer explained the swift charge collection. Finally, 9p-3PACz PSCs achieved a high PCE of 16.52% with a bandgap of 1.77 eV. This work provides valuable guidance for designing more effective HTL modification materials.

EXPERIMENTAL SECTION

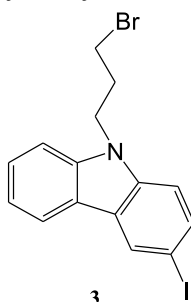
Materials. All the chemical reagents (powder and solution) were used as obtained and no further processing. Xi'an Polymer Light Technology Corp. provided the HTL (PTAA). Advanced Election Technology CO. supplied the PbBr_2 , FAI , PbI_2 , and CsI . Tokyo Chemical Industry Co., Ltd. provided the Guanidine bromide (GuBr). CsBr , BCP, C60, Carbazole, 1,3-dibromo propane, triethyl phosphite, 9-[4-(4,4,5,5-Tetramethyl-1,3,2-dioxaborolan-2-yl)-phenyl]carbazole, methoxyppyridinylboronic acid, bis-(triphenylphosphine)palladium(II) dichloride, 1,4-ioxacyclohexane,

acetone, tetrahydrofuran, KOH, and all solutions purchased from Sigma-Aldrich. [3-(3-iodocarbazol-9-yl)propyl]phosphonic acid (I-3PACz), (3-(3-[4-(carbazol-9-yl)phenyl]carbazol-9-yl)propyl)phosphonic acid (9p-3PACz), and (3-[3-(2-methoxyppyridin-3-yl)carbazol-9-yl]propyl)phosphonic acid (2M3P-3PACz) synthesized as new derivatives according to the description presented in Supporting Information (Scheme S1).

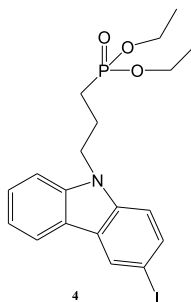
Experimental Details of the Synthesis.



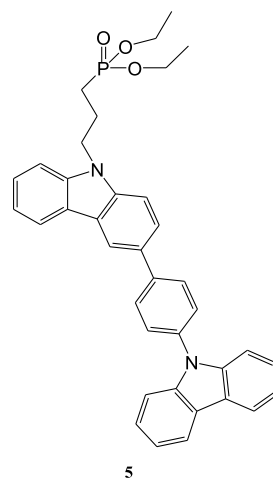
3-Iodocarbazole (**2**) was prepared from carbazole using the Tucker iodination with KI/KIO₃ in CH₃COOH.⁵⁶



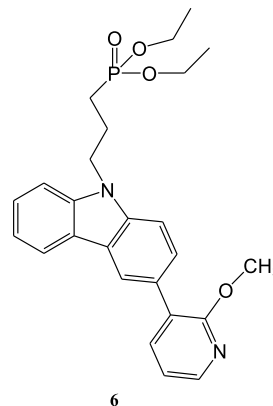
The alkylation reaction obtained 9-(3-bromopropyl)-3-iodo-9H-carbazole (**3**). Specifically, 1,3-dibromo propane was chosen as the alkylation agent, and KOH was the source of the base.⁵⁷ MS (APCI+, 20 V): 413.53 ([M + H], 100%). ¹H NMR (400 MHz, CDCl₃-d₆, δ): 8.42 (s, 1H, Ar), 8.05 (d, 1H, *JJ* = 7.6 Hz, Ar), 7.74 (d, 1H, *JJ* = 8.8 Hz, Ar), 7.54–7.48 (m, 2H, Ar), 7.32–7.27 (m, 2H, Ar), 4.49 (t, 2H, *J* = 6.8, CH₂), 3.38 (t, 2H, *JJ* = 6 Hz, CH₂), 2.51–2.36 (m, 2H, CH₂).



Diethyl [3-(3-iodocarbazol-9-yl)propyl]phosphonate (**4**). First, 2 g (4.84 mmol) of 9-(3-bromopropyl)-3-iodo-9H-carbazole (**3**) was dissolved in 2.48 mL of phosphorous acid triethyl. Then, the reaction mixture was heated to reflux for 24 h. With the control of TLC, the crude product was purified and washed by silica gel column chromatography. Meanwhile, the mixture of tetrahydrofuran and hexane has a volume ratio of 2:1 as the eluent. Finally, the product yield is 75% (1.5 g of colorless resin). MS (APCI+, 20 V): 472.27 ([M + H], 100%). ¹H NMR (400 MHz, DMSO-*d*₆, δ): 8.56 (s, 1H, Ar), 8.20 (d, 1H, *JJ* = 7.6 Hz, Ar), 7.72 (d, 1H, *JJ* = 8.4 Hz, Ar), 7.66 (d, 1H, *JJ* = 8 Hz, Ar), 7.55–7.43 (m, 2H, Ar), 7.22 (t, 1H, *JJ* = 7.2 Hz, Ar), 4.47 (t, 2H, *JJ* = 7.8 Hz, NCH₂), 4.02–3.91 (m, 4H, 2x CH₂), 1.99–1.89 (m, 2H, CH₂), 1.78–1.70 (m, 2H, CH₂), 1.22–1.14 (m, 6H, 2x CH₃).

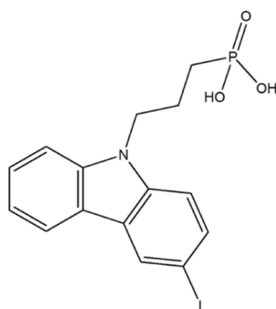


Diethyl (3-[3-[4-(carbazol-9-yl)phenyl]carbazol-9-yl]propyl)phosphonate (**5**). Diethyl [3-(3-iodocarbazol-9-yl)propyl]phosphonate (**4**) (0.50 g, 1.06 mmol), 9-[4-(4,4,5,5-Tetramethyl-1,3,2-dioxaborolan-2-yl)phenyl]carbazole (0.58 g, 1.57 mmol), bis-(triphenylphosphine)palladium(II) chloride (PdCl₂(PPh₃)₂) (0.03 g, 0.07 mmol) and the powdered of potassium hydroxide (0.29 g, 5.16 mmol) were stirred in 7 mL of tetrahydrofuran containing 0.7 mL of degassed water and reflux in a filled nitrogen atmosphere for 3 h. With the control of TLC, we used chlorobenzene as an extractant to obtain the product by mixing the reactants and pouring them into ice water. Anhydrous Na₂SO₄ was used to dry the organic fraction. Crude product was purified and washed by silica gel column chromatography. Meanwhile, the eluent is a mixture of tetrahydrofuran and hexane with a volume ratio of 4:1. Finally, the product yield is 80% (0.4 g of colorless resin). MS (APCI+, 20 V): 587.24 ([M + H], 100%). ¹H NMR (400 MHz, DMSO-*d*₆, δ): 8.31 (s, 1H, Ar), 8.09–8.06 (m, 3H, Ar), 7.82 (d, 2H, *JJ* = 8 Hz, Ar), 7.69 (d, 1H, *J* = 8.4 Hz, Ar), 7.55 (d, 2H, *JJ* = 8 Hz, Ar), 7.45–7.32 (m, 7H, Ar), 7.21 (m, 3H, Ar), 4.35 (t, 2H, *JJ* = 7.8 Hz, NCH₂), 4.00–3.96 (m, 4H, 2x OCH₂), 2.20–2.11 (m, 2H, CH₂), 1.77–1.63 (m, 2H, CH₂), 1.21–1.18 (m, 6H, 2x CH₃).

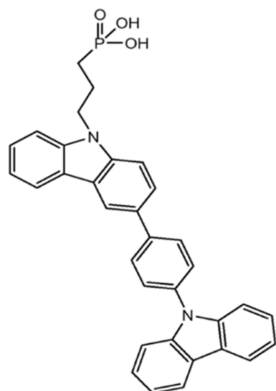


Diethyl (3-[3-(2-methoxyppyridin-3-yl)-9H-carbazol-9-yl]propyl)phosphonate (**6**). Diethyl [3-(3-iodocarbazol-9-yl)propyl]phosphonate (**4**) (0.48 g, 1.02 mmol), methoxyppyridinylboronic acid (0.23 g, 1.50 mmol), bis(triphenylphosphine)palladium(II) chloride (PdCl₂(PPh₃)₂) (0.03 g, 0.07 mmol) and the powdered of potassium hydroxide (0.29 g, 5.16 mmol) were stirred in 7 mL of tetrahydrofuran containing 0.7 mL of degassed water and reflux in a filled nitrogen atmosphere for 3 h. With the control of TLC, we used chlorobenzene as an extractant to obtain the product by mixing the reactants and pouring them into ice water. Anhydrous Na₂SO₄ was used to dry the organic fraction. Crude product was purified and washed by silica gel column chromatography. Meanwhile, the eluent is a mixture of tetrahydrofuran and hexane with a volume ratio of 4:1. Finally, the product yield is 7% (0.35 g of colorless resin). MS (APCI+, 20 V): 453.32 ([M + H], 100%). ¹H NMR (400 MHz, DMSO-*d*₆,

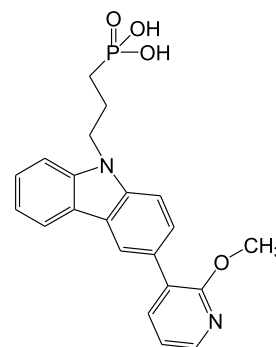
δ): 8.45 (s, 1H, Ar), 8.25–8.14 (m, 2H, Ar), 7.77–7.61 (m, 3H, Ar), 7.49–7.42 (m, 1H, Ar), 7.28–7.16 (m, 1H, Ar), 7.2 (t, 1H, $J = 7.6$ Hz, Ar), 6.41 (t, 1H, $J = 6.8$ Hz, Ar), 4.56–4.48 (m, 3H, OCH₃), 4.06–3.94 (m, 4H, 2x OCH₂), 3.92–3.90 (m, 2H, CH₂), 2.07–1.95 (m, 2H, CH₂), 1.63–1.49 (m, 2H, CH₂), 1.22–1.10 (m, 6H, 2x CH₃).



[3-(3-iodocarbazol-9-yl)propyl]phosphonic acid (I-3PACz). Compound 4 (0.50 g, 1.21 mmol) was dissolved in 15 mL of 1,4-ioxacyclohexane. Then, the trimethylsilyl bromide (TMBS) (2.96 g, 19.37 mmol) was added to the above solution. Then, the mixture was stirred at room temperature for 24 h and poured into the mixture of methanol and water. The resulting precipitate was filtered. Finally, the product yield is 70% (0.35 g of blue product). MS (APCI+, 20 V): 416.17 ([M + H], 100%). ¹H NMR (400 MHz, DMSO-*d*₆, δ): 8.52 (s, 1H, Ar), 8.22–8.11 (m, 1H, Ar), 7.75–7.58 (m, 2H, Ar), 7.55–7.42 (m, 2H, Ar), 7.26–7.15 (m, 1H, Ar), 5.04–4.72 (m, 2H, 2 × OH), 4.43 (t, 2H, $J = 7.6$ Hz, NCH₂), 1.95 (m, 2H, $J = 7.8$ Hz, PCH₂), 1.61–1.47 (m, 2H, CH₂). ¹³C NMR (400 MHz, DMSO-*d*₆, δ): 140.44, 140.40, 139.59, 134.04, 129.20, 127.03, 126.24, 125.19, 122.46, 121.24, 120.74, 119.81, 119.27, 112.36, 109.97, 109.73, 82.15, 43.08, 25.94, 22.96.



(3-(3-[4-(carbazol-9-yl)phenyl]carbazol-9-yl)propyl)phosphonic acid (9p-3PACz). Compound 5 (0.43 g, 0.73 mmol) was dissolved in anhydrous 1,4-ioxacyclohexane (10 mL) under the argon-filled atmosphere, followed by dropwise addition of trimethylsilyl bromide (TMBS) (1.54 mL, 11.64 mmol). The reaction was stirred for 24 h at 25 °C. Afterward, 10 mL of methanol was added, and stirring continued for 3 h. Finally, distilled water was added dropwise (20 mL) until the solution became opaque and stirred overnight. The precipitated product was filtered off and washed with water to give 0.32 g (75%) dark powder. MS (APCI+, 20 V): 531.18 ([M + H], 100%). ¹H NMR (400 MHz, DMSO-*d*₆, δ): 8.69 (s, 1H, Ar), 8.36–8.32 (m, 3H, Ar), 8.14 (d, 2H, $J = 8$ Hz, Ar), 7.96 (d, 1H, $J = 8.4$ Hz, Ar), 7.86–7.74 (m, 5H, Ar), 7.60–7.50 (m, 6H, Ar), 7.38–7.29 (m, 3H, Ar), 4.60 (t, 2H, NCH₂), 2.18–2.01 (m, 2H, CH₂), 1.69–1.61 (m, 2H, CH₂). ¹³C NMR (100 MHz, DMSO-*d*₆, δ): 141.03, 140.83, 140.66, 140.23, 139.68, 135.68, 130.76, 128.75, 127.53, 126.77, 126.55, 125.39, 125.28, 123.23, 122.76, 121.15, 121.05, 120.53, 119.52, 119.17, 110.38, 110.19, 110.03, 67.49, 30.89, 23.20.



(3-[3-(2-methoxy-pyridin-3-yl)carbazol-9-yl]propyl)phosphonic acid (2M3P-3PACz). Diethyl (3-(3-(2-methoxy-pyridin-9-yl)-9H-carbazol-9-yl)propyl)phosphonate 6 (0.35 g, 0.77 mmol) was dissolved in anhydrous 1,4-ioxacyclohexane (10 mL) under argon atmosphere followed by dropwise addition of trimethylsilyl bromide (TMBS) (1.62 mL, 12.34 mmol). The reaction was stirred for 24 h at 25 °C. Afterward, 10 mL of methanol was added to the above system, stirring for 3 h. Finally, distilled water was added dropwise (20 mL) until the solution became opaque and stirred overnight. The precipitated product was filtered off and washed with water to give 0.25 g (71%) of bright powder. MS (APCI+, 20 V): 397.12 ([M + H], 100%). ¹H NMR (400 MHz, DMSO-*d*₆, δ): 8.51 (s, 1H, Ar), 8.21–8.11 (m, 2H, Ar), 7.89–7.62 (m, 5H, Ar), 7.52–7.42 (m, 1H, Ar), 7.39–7.37 (m, 1H, Ar), 7.2 (t, 1H, $J = 7.6$ Hz, Ar), 6.34 (t, 1H, $J = 6.8$ Hz, Ar), 4.56–4.48 (m, 3H, OCH₃), 3.92–3.90 (m, 2H, CH₂), 2.07–1.95 (m, 2H, CH₂), 1.63–1.49 (m, 2H, CH₂). ¹³C NMR (100 MHz, DMSO-*d*₆, δ): 162.12, 140.79, 139.87, 138.62, 134.15, 131.41, 127.50, 126.88, 126.21, 122.73, 120.77, 120.49, 119.37, 118.01, 109.89, 109.13, 106.13, 53.79, 30.89, 26.13, 23.13.

Device Fabrication. Perovskite Precursor Solution. FA_{0.8}Cs_{0.2}PbI_{1.8}Br_{1.2} was prepared by dissolving FAI (0.576 mol), CsI (0.144 mol), FABr (0.384 mol), PbI₂ (0.720 mol), PbBr₂ (0.480 mol), and CsBr (0.096 mol) in the 1 mL of DMSO/DMF (1/4, v/v) mixture. Before use, the solution was filtered by a 0.22 μ m PTFE membrane.

Wide Bandgap Perovskite Solar Cell Fabrication. The ITO was cleaned with water and isopropanol, followed by drying. The clean ITO was treated by plasma for 5 min (Low-Pressure Plasma System Diener electronic: FEMTO, Soft Pressure Plasma Etching: SEDEGE). After cooling to room temperature, the ITO was transferred to the glove box. PTAA (1.5 mg dissolved in 1 mL toluene) was spin-coated on the ITO in 2000 r.p.m. for 30 s. Then, the ITO was annealed on the hotplate at 100 °C for 10 min. For monomolecular layer passivation, the molecule (dissolved in DMF) was spin-coated on the PTAA layer at 5000 r.p.m. for 30 s and annealed at 100 °C for 5 min. The surface was washed with DMF to remove unbonded sample molecules and to leave only the monomolecular layer on the PTAA surface. Then, the perovskite was deposited on the substrate with the speed of (1) 2000 r.p.m. for the 10 s and (2) 6000 r.p.m. for the 40 s. 150 μ L CB was dropped at 30 s. Then, the film was placed on the hotplate and baked at 100 °C for 15 min. After cooling down to room temperature, GuBr (0.5 mg/mL in IPA, 5000 r.p.m. for the 30 s) was spin-coated for the surface passivation of the PVK layer. Then, C60 (20 nm), BCP (7 nm), and Ag (100 nm) were deposited on the substrate by thermal evaporation (ALS Technology Co., Ltd. E-200) under a vacuum of 10⁻⁵ Pa using a shadow mask.

Characterization. X-ray diffraction patterns were performed using the XRD (Rigaku, Japan, SmartLab). PSCs photovoltaic parameters were measured by the Keithley 2611A source meter and a solar simulator under 100 mWcm⁻² AM 1.5G illumination in ambient air conditions (Bunkouki CEP-2000SRR). IPCE spectra were obtained using a monochromatic Xenon lamp (Bunkouki CEP-2000SRR). MS curves, EIS, TPC, and TPV results were all performed using PAIOS equipment. The valence band was estimated from a photoelectron yield measurement system (PYS, BUNKOKEIKI, KV-205 HK). SEM (FE-SEM, JEOL JSM-6340) was used to check the surface morphology of the perovskite film. The PL and TRPL were measured

using a Hamamatsu photonics K.K. Co., Japan, Quantaaurus-Tau. Fermi level measurements were performed using FAC-2 (RIKEN KEIKI Co. Ltd.).

Geometrical parameters of PTAA in the DFT framework were obtained from the QUANTUM ESPRESSO software.^{58,59} The polymers were considered a monomer unit in the calculation. The atoms and ions were placed in the free cell with parameters long enough to ignore the interaction between the monomer units. In addition, Gaussian software carried out geometrical parameters of I-3PACz, 9p-3PACz, and 2M3P-3PACz.⁶⁰ PBE1PBE/def2-TZVP level of theory using the Gaussian program to evaluate the properties of molecules in specific conformations. Multiwfn 3.8(dev) is used to generate and analyze calculation results.⁶¹

■ ASSOCIATED CONTENT

SI Supporting Information

The Supporting Information is available free of charge at <https://pubs.acs.org/doi/10.1021/acsami.3c08655>.

The perovskite solution contact angle of the different substrates, SEM images, and XRD of the perovskite film deposited on different substrates. UV-vis of the perovskite film. Dark *I*-*V* curves of the devices. PL and TRPL curves. The energy level of the film and Gaussian calculation. EIS and Mott-Schottky plots of control and target devices. Statistics of photovoltaic PSCs prepared on different substrates (PDF)

■ AUTHOR INFORMATION

Corresponding Authors

Huan Bi – *i*-Powered Energy System Research Center (*i*-PERC), The University of Electro-Communications, Chofu 182-8585 Tokyo, Japan; Graduate School of Informatics and Engineering, The University of Electro-Communications, Chofu 182-8585 Tokyo, Japan; orcid.org/0000-0001-7680-9816; Email: hbi.trans.sci@gmail.com

Saulius Grigalevicius – Department of Polymers Chemistry and Technology, Kaunas University of Technology, Kaunas LTS0254, Lithuania; Email: saulius.grigalevicius@ktu.lt

Qing Shen – *i*-Powered Energy System Research Center (*i*-PERC), The University of Electro-Communications, Chofu 182-8585 Tokyo, Japan; Graduate School of Informatics and Engineering, The University of Electro-Communications, Chofu 182-8585 Tokyo, Japan; orcid.org/0000-0001-8359-3275; Email: shen@pc.uec.ac.jp

Shuzi Hayase – *i*-Powered Energy System Research Center (*i*-PERC), The University of Electro-Communications, Chofu 182-8585 Tokyo, Japan; Graduate School of Informatics and Engineering, The University of Electro-Communications, Chofu 182-8585 Tokyo, Japan; orcid.org/0000-0001-8192-5336; Email: hayase@uec.ac.jp

Authors

Jiaqi Liu – *i*-Powered Energy System Research Center (*i*-PERC), The University of Electro-Communications, Chofu 182-8585 Tokyo, Japan

Raminta Beresneviciute – Department of Polymers Chemistry and Technology, Kaunas University of Technology, Kaunas LTS0254, Lithuania

Daiva Tavgeniene – Department of Polymers Chemistry and Technology, Kaunas University of Technology, Kaunas LTS0254, Lithuania

Zheng Zhang – *i*-Powered Energy System Research Center (*i*-PERC), The University of Electro-Communications, Chofu 182-8585 Tokyo, Japan; Graduate School of Informatics and

Engineering, The University of Electro-Communications, Chofu 182-8585 Tokyo, Japan

Liang Wang – *i*-Powered Energy System Research Center (*i*-PERC), The University of Electro-Communications, Chofu 182-8585 Tokyo, Japan

Gaurav Kapil – *i*-Powered Energy System Research Center (*i*-PERC), The University of Electro-Communications, Chofu 182-8585 Tokyo, Japan

Chao Ding – Graduate School of Informatics and Engineering, The University of Electro-Communications, Chofu 182-8585 Tokyo, Japan

Shahrir Razey Sahamir – *i*-Powered Energy System Research Center (*i*-PERC), The University of Electro-Communications, Chofu 182-8585 Tokyo, Japan; orcid.org/0000-0002-9167-5980

Yoshitaka Sanehira – *i*-Powered Energy System Research Center (*i*-PERC), The University of Electro-Communications, Chofu 182-8585 Tokyo, Japan; orcid.org/0000-0003-2030-2690

Ajay Kumar Baranwal – *i*-Powered Energy System Research Center (*i*-PERC), The University of Electro-Communications, Chofu 182-8585 Tokyo, Japan; orcid.org/0000-0003-4582-4532

Takeshi Kitamura – *i*-Powered Energy System Research Center (*i*-PERC), The University of Electro-Communications, Chofu 182-8585 Tokyo, Japan; orcid.org/0009-0005-2782-4549

Dandan Wang – Graduate School of Informatics and Engineering, The University of Electro-Communications, Chofu 182-8585 Tokyo, Japan

Yuyao Wei – Graduate School of Informatics and Engineering, The University of Electro-Communications, Chofu 182-8585 Tokyo, Japan

Yongge Yang – Graduate School of Informatics and Engineering, The University of Electro-Communications, Chofu 182-8585 Tokyo, Japan

Dong-Won Kang – School of Energy Systems Engineering, Chung-Ang University, Seoul 06974, Republic of Korea; orcid.org/0000-0002-4818-8108

Complete contact information is available at:

<https://pubs.acs.org/doi/10.1021/acsami.3c08655>

Author Contributions

H.B.: Conceived the idea and designed the experiments; fabricated the devices and conduct the characterization; carried out the DFT calculation; data analysis and discussion; wrote draft of manuscript and revised manuscripts. J.L.: conducted the DFT calculation and provided constructive suggestions for the manuscript. R.B.: synthesized the *x*-3PACz-based materials and related tests. D.T.: synthesized the *x*-3PACz-based materials and related tests. Zheng Zhang: Data analysis and discussion. L.W.: data analysis and discussion. G.K.: data analysis and discussion. C.D.: data analysis and discussion; PL and TRPL testing. S.R.S.: data analysis and discussion. Y.S.: data analysis and discussion. A.K.B.: data analysis and discussion. T.K.: data analysis and discussion. D.W.: data analysis and discussion; PL and TRPL testing. Y.W.: data analysis and discussion; PL and TRPL testing. Y.Y.: data analysis and discussion; PL and TRPL testing. D.-W.K.: supported and supervised the project. S.G.: synthesized the *x*-3PACz-based materials and related tests; supported and supervised the project. Q.S.: supported and supervised the

project. S.H.: conceived the idea and designed the experiments; supported and supervised the project; wrote draft of manuscript and revised manuscripts.

Notes

The authors declare no competing financial interest.

ACKNOWLEDGMENTS

This work was partially supported by the New Energy and Industrial Technology Development (JPNP20015) and JSPS (JPJSBP120224201). This work was also supported by project S-LJB-22-2 from the Research Council of Lithuania.

REFERENCES

- (1) NREL. *Best Research-Cell Efficiency Chart*, 2021. <https://www.nrel.gov/pv/cell-efficiency.html>.
- (2) Jošt, M.; Köhnen, E.; Al-Ashouri, A.; Bertram, T.; Tomšič, Š.; Magomedov, A.; Kasparavicius, E.; Kodalle, T.; Lipovšek, B.; Getautis, V.; Schlattmann, R.; Kaufmann, C. A.; Albrecht, S.; Topič, M. Perovskite/CIGS Tandem Solar Cells: From Certified 24.2% toward 30% and Beyond. *ACS Energy Lett.* **2022**, *7*, 1298–1307.
- (3) Li, H.; Wang, Y.; Gao, H.; Zhang, M.; Lin, R.; Wu, P.; Xiao, K.; Tan, H. Revealing the Output Power Potential of Bifacial Monolithic All-Perovskite Tandem Solar Cells. *eLight* **2022**, *2*, 21.
- (4) Lin, R.; Xu, J.; Wei, M.; Wang, Y.; Qin, Z.; Liu, Z.; Wu, J.; Xiao, K.; Chen, B.; Park, S. M.; Chen, G.; Atapattu, H. R.; Graham, K. R.; Xu, J.; Zhu, J.; Li, L.; Zhang, C.; Sargent, E. H.; Tan, H. All-Perovskite Tandem Solar Cells with Improved Grain Surface Passivation. *Nature* **2022**, *603*, 73–78.
- (5) Gao, Y.; Lin, R.; Xiao, K.; Luo, X.; Wen, J.; Yue, X.; Tan, H. Performance Optimization of Monolithic All-Perovskite Tandem Solar Cells under Standard and Real-World Solar Spectra. *Joule* **2022**, *6*, 1944.
- (6) Shankar, G.; Kumar, P.; Pradhan, B. All-Perovskite Two-Terminal Tandem Solar Cell with 32.3% Efficiency by Numerical Simulation. *Mater. Today Sus* **2022**, *20*, 100241.
- (7) Yang, Z.; Yu, Z.; Wei, H.; Xiao, X.; Ni, Z.; Chen, B.; Deng, Y.; Habisreutinger, S. N.; Chen, X.; Wang, K.; Zhao, J.; Rudd, P. N.; Berry, J. J.; Beard, M. C.; Huang, J. Enhancing Electron Diffusion Length in Narrow-Bandgap Perovskites for Efficient Monolithic Perovskite Tandem Solar Cells. *Nat. Commun.* **2019**, *10*, 4498.
- (8) He, R.; Yi, Z.; Luo, Y.; Luo, J.; Wei, Q.; Lai, H.; Huang, H.; Zou, B.; Cui, G.; Wang, W.; Xiao, C.; Ren, S.; Chen, C.; Wang, C.; Xing, G.; Fu, F.; Zhao, D. Pure 2d Perovskite Formation by Interfacial Engineering Yields a High Open-Circuit Voltage Beyond 1.28 V for 1.77-EV Wide-Bandgap Perovskite Solar Cells. *Adv. Sci.* **2022**, *9*, 2203210.
- (9) Kuan, C.-H.; Luo, G.-S.; Narra, S.; Maity, S.; Hiramatsu, H.; Tsai, Y.-W.; Lin, J.-M.; Hou, C.-H.; Shyue, J.-J.; Wei-Guang Diao, E. How Can a Hydrophobic Polymer Ptaa Serve as a Hole-Transport Layer for an Inverted Tin Perovskite Solar Cell? *Chem. Eng. J.* **2022**, *450*, 138037.
- (10) Luo, J.; Xia, J.; Yang, H.; Malik, H. A.; Han, F.; Shu, H.; Yao, X.; Wan, Z.; Jia, C. Novel Approach toward Hole-Transporting Layer Doped by Hydrophobic Lewis Acid through Infiltrated Diffusion Doping for Perovskite Solar Cells. *Nano Energy* **2020**, *70*, 104509.
- (11) Li, Y.; Liang, C.; Wang, G.; Li, J.; Chen, S.; Yang, S.; Xing, G.; Pan, H. Two-Step Solvent Post-Treatment on Ptaa for Highly Efficient and Stable Inverted Perovskite Solar Cells. *Photon. Res.* **2020**, *8*, A39.
- (12) Zheng, X.; Chen, B.; Dai, J.; Fang, Y.; Bai, Y.; Lin, Y.; Wei, H.; Zeng, X. C.; Huang, J. Defect Passivation in Hybrid Perovskite Solar Cells Using Quaternary Ammonium Halide Anions and Cations. *Nat. Energy* **2017**, *2*, 17102.
- (13) Tian, S.; Chen, J.; Lian, X.; Wang, Y.; Zhang, Y.; Yang, W.; Wu, G.; Qiu, W.; Chen, H. Engineering the Underlying Surface to Manipulate the Growth of 2D Perovskites for Highly Efficient Solar Cells. *J. Mater. Chem. A* **2019**, *7*, 14027–14032.
- (14) Lim, K.-G.; Ahn, S.; Lee, T.-W. Energy Level Alignment of Dipolar Interface Layer in Organic and Hybrid Perovskite Solar Cells. *J. Mater. Chem. C* **2018**, *6*, 2915–2924.
- (15) Wang, S.; Sakurai, T.; Wen, W.; Qi, Y. Energy Level Alignment at Interfaces in Metal Halide Perovskite Solar Cells. *Adv. Mater. Interfaces* **2018**, *5*, 1800260.
- (16) Zheng, S.; Wang, G.; Liu, T.; Lou, L.; Xiao, S.; Yang, S. Materials and Structures for the Electron Transport Layer of Efficient and Stable Perovskite Solar Cells. *Sci. China Chem.* **2019**, *62*, 800–809.
- (17) Shao, S.; Loi, M. A. The Role of the Interfaces in Perovskite Solar Cells. *Adv. Mater. Interfaces* **2020**, *7*, 1901469.
- (18) Xu, J.; Dai, J.; Dong, H.; Li, P.; Chen, J.; Zhu, X.; Wang, Z.; Jiao, B.; Hou, X.; Li, J.; Wu, Z. Surface-Tension Release in Ptaa-Based Inverted Perovskite Solar Cells. *Org. Electron.* **2022**, *100*, 106378.
- (19) Wang, J.; Xu, J.; Li, Z.; Lin, X.; Yu, C.; Wu, H.; Wang, H.-I. Front-Contact Passivation of Pin MAPbI₃ Solar Cells with Superior Device Performances. *ACS Appl. Energy Mater.* **2020**, *3*, 6344–6351.
- (20) Cho, A.-N.; Park, N.-G. Impact of Interfacial Layers in Perovskite Solar Cells. *ChemSusChem* **2017**, *10*, 3687–3704.
- (21) Guan, L.; Yu, L.; Wu, L.; Zhang, S.; Lin, Y.; Jiao, Y.; Zhang, S.; Zhao, F.; Ren, Y.; Zhou, X.; Liu, Z. Grain Size Control of Perovskite Films Based on B-Alanine Self-Assembled Monolayers Surface Treatment. *Thin Solid Films* **2021**, *732*, 138770.
- (22) Ali, F.; Roldán-Carmona, C.; Sohail, M.; Nazeeruddin, M. K. Applications of Self-Assembled Monolayers for Perovskite Solar Cells Interface Engineering to Address Efficiency and Stability. *Adv. Energy Mater.* **2020**, *10*, 2002989.
- (23) Lin, Y.; Zhang, Y.; Zhang, J.; Marcinkas, M.; Malinauskas, T.; Magomedov, A.; Nugraha, M. I.; Kaltsas, D.; Naphade, D. R.; Harrison, G. T.; El-Labban, A.; Barlow, S.; De Wolf, S.; Wang, E.; McCulloch, I.; Tsetseris, L.; Getautis, V.; Marder, S. R.; Anthopoulos, T. D. 18.9% Efficient Organic Solar Cells Based on N-Doped Bulk-Heterojunction and Halogen-Substituted Self-Assembled Monolayers as Hole Extracting Interlayers. *Adv. Energy Mater.* **2022**, *12*, 2202503.
- (24) Li, L.; Wang, Y.; Wang, X.; Lin, R.; Luo, X.; Liu, Z.; Zhou, K.; Xiong, S.; Bao, Q.; Chen, G.; Tian, Y.; Deng, Y.; Xiao, K.; Wu, J.; Saidaminov, M. I.; Lin, H.; Ma, C.-Q.; Zhao, Z.; Wu, Y.; Zhang, L.; Tan, H. Flexible All-Perovskite Tandem Solar Cells Approaching 25% Efficiency with Molecule-Bridged Hole-Selective Contact. *Nat. Energy* **2022**, *7*, 708–717.
- (25) Kapil, G.; Bessho, T.; Sanehira, Y.; Sahamir, S. R.; Chen, M.; Baranwal, A. K.; Liu, D.; Sono, Y.; Hirotsani, D.; Nomura, D.; Nishimura, K.; Kamarudin, M. A.; Shen, Q.; Segawa, H.; Hayase, S. Tin–Lead Perovskite Solar Cells Fabricated on Hole Selective Monolayers. *ACS Energy Lett.* **2022**, *7*, 966–974.
- (26) Ali, F.; Roldán-Carmona, C.; Sohail, M.; Nazeeruddin, M. K. Applications of Self-Assembled Monolayers for Perovskite Solar Cells Interface Engineering to Address Efficiency and Stability. *Adv. Energy Mater.* **2020**, *10*, 2002989.
- (27) Qu, Z.; Ma, F.; Zhao, Y.; Chu, X.; Yu, S.; You, J. Updated Progresses in Perovskite Solar Cells. *Chin. Phys. Lett.* **2021**, *38*, 107801.
- (28) Yao, Y.; Cheng, C.; Zhang, C.; Hu, H.; Wang, K.; De Wolf, S. Organic Hole-Transport Layers for Efficient, Stable, and Scalable Inverted Perovskite Solar Cells. *Adv. Mater.* **2022**, *34*, 2203794.
- (29) Kapil, G.; Ripolles, T. S.; Hamada, K.; Ogomi, Y.; Bessho, T.; Kinoshita, T.; Chantana, J.; Yoshino, K.; Shen, Q.; Toyoda, T.; Minemoto, T.; Murakami, T. N.; Segawa, H.; Hayase, S. Highly Efficient 17.6% Tin–Lead Mixed Perovskite Solar Cells Realized through Spike Structure. *Nano Lett.* **2018**, *18*, 3600–3607.
- (30) Tan, Y.; Chang, X.; Zhong, J.-X.; Feng, W.; Yang, M.; Tian, T.; Gong, L.; Wu, W.-Q. Chemical Linkage and Passivation at Buried Interface for Thermally Stable Inverted Perovskite Solar Cells with Efficiency over 22%. *CCS Chem.* **2023**, *5*, 1802–1814.
- (31) Bi, H.; Zuo, X.; Liu, B.; He, D.; Bai, L.; Wang, W.; Li, X.; Xiao, Z.; Sun, K.; Song, Q.; Zang, Z.; Chen, J. Multifunctional Organic Ammonium Salt-Modified SnO₂ Nanoparticles toward Efficient and

Stable Planar Perovskite Solar Cells. *J. Mater. Chem. A* **2021**, *9*, 3940–3951.

(32) Chen, W.; Zhu, Y.; Xiu, J.; Chen, G.; Liang, H.; Liu, S.; Xue, H.; Birgersson, E.; Ho, J. W.; Qin, X.; Lin, J.; Ma, R.; Liu, T.; He, Y.; Ng, A. M.-C.; Guo, X.; He, Z.; Yan, H.; Djurišić, A. B.; Hou, Y. Monolithic Perovskite/Organic Tandem Solar Cells with 23.6% Efficiency Enabled by Reduced Voltage Losses and Optimized Interconnecting Layer. *Nat. Energy* **2022**, *7*, 229–237.

(33) Yu, Z.; Chen, X.; Harvey, S. P.; Ni, Z.; Chen, B.; Chen, S.; Yao, C.; Xiao, X.; Xu, S.; Yang, G.; Yan, Y.; Berry, J. J.; Beard, M. C.; Huang, J. Gradient Doping in Sn-Pb Perovskites by Barium Ions for Efficient Single-Junction and Tandem Solar Cells. *Adv. Mater.* **2022**, *34*, No. e2110351.

(34) Huo, X.; Li, Y.; Lu, Y.; Dong, J.; Zhang, Y.; Zhao, S.; Qiao, B.; Wei, D.; Song, D.; Xu, Z. Suppressed Halide Segregation and Defects in Wide Bandgap Perovskite Solar Cells Enabled by Doping Organic Bromide Salt with Moderate Chain Length. *J. Phys. Chem. C* **2022**, *126*, 1711–1720.

(35) Yuan, Y.; Huang, J. Ion Migration in Organometal Trihalide Perovskite and Its Impact on Photovoltaic Efficiency and Stability. *Acc. Chem. Res.* **2016**, *49*, 286–293.

(36) Chen, J.; Park, N. G. Causes and Solutions of Recombination in Perovskite Solar Cells. *Adv. Mater.* **2019**, *31*, No. e1803019.

(37) Li, Y. M.; Chen, Z. J.; Yu, B. C.; Tan, S.; Cui, Y. Q.; Wu, H. J.; Luo, Y. H.; Shi, J. J.; Li, D. M.; Meng, Q. B. Efficient, Stable Formamidinium-Cesium Perovskite Solar Cells and Minimodules Enabled by Crystallization Regulation. *Joule* **2022**, *6*, 676–689.

(38) An, Q.; Paulus, F.; Becker-Koch, D.; Cho, C.; Sun, Q.; Weu, A.; Bitton, S.; Tessler, N.; Vaynzof, Y. Small Grains as Recombination Hot Spots in Perovskite Solar Cells. *Matter* **2021**, *4*, 1683–1701.

(39) Abate, S. Y.; Huang, D.-C.; Tao, Y.-T. Surface Modification of TiO_2 Layer with Phosphonic Acid Monolayer in Perovskite Solar Cells: Effect of Chain Length and Terminal Functional Group. *Org. Electron.* **2020**, *78*, 105583.

(40) Canil, L.; Cramer, T.; Fraboni, B.; Ricciarelli, D.; Meggiolaro, D.; Singh, A.; Liu, M.; Rusu, M.; Wolff, C. M.; Phung, N.; Wang, Q.; Neher, D.; Unold, T.; Vivo, P.; Gagliardi, A.; De Angelis, F.; Abate, A. Tuning Halide Perovskite Energy Levels. *Energy Environ. Sci.* **2021**, *14*, 1429–1438.

(41) Ding, C.; Zhang, Y.; Liu, F.; Kitabatake, Y.; Hayase, S.; Toyoda, T.; Yoshino, K.; Minemoto, T.; Katayama, K.; Shen, Q. Effect of the Conduction Band Offset on Interfacial Recombination Behavior of the Planar Perovskite Solar Cells. *Nano Energy* **2018**, *53*, 17–26.

(42) Minemoto, T.; Matsui, T.; Takakura, H.; Hamakawa, Y.; Negami, T.; Hashimoto, Y.; Uenoyama, T.; Kitagawa, M. Theoretical Analysis of the Effect of Conduction Band Offset of Window/CIS Layers on Performance of CIS Solar Cells Using Device Simulation. *Sol. Energy Mater. Sol. Cells* **2001**, *67*, 83–88.

(43) Minemoto, T.; Murata, M. Theoretical Analysis on Effect of Band Offsets in Perovskite Solar Cells. *Sol. Energy Mater. Sol. Cells* **2015**, *133*, 8–14.

(44) Caprioglio, P.; Wolff, C. M.; Sandberg, O. J.; Armin, A.; Rech, B.; Albrecht, S.; Neher, D.; Stolterfoht, M. On the Origin of the Ideality Factor in Perovskite Solar Cells. *Adv. Energy Mater.* **2020**, *10*, 2000502.

(45) Liu, C.; Igci, C.; Yang, Y.; Syzgantseva, O. A.; Syzgantseva, M. A.; Rakstys, K.; Kanda, H.; Shibayama, N.; Ding, B.; Zhang, X.; Jankauskas, V.; Ding, Y.; Dai, S.; Dyson, P. J.; Nazeeruddin, M. K. Dopant-Free Hole Transport Materials Afford Efficient and Stable Inorganic Perovskite Solar Cells and Modules. *Angew Chem. Int. Ed. Engl.* **2021**, *60*, 20489–20497.

(46) Bi, H.; Guo, Y.; Guo, M.; Ding, C.; Hayase, S.; Mou, T.; Shen, Q.; Han, G.; Hou, W. Highly Efficient and Low Hysteresis Methylammonium-Free Perovskite Solar Cells Based on Multifunctional Oteracil Potassium Interface Modification. *Chem. Eng. J.* **2022**, *439*, 135671.

(47) Bi, H.; Liu, B.; He, D.; Bai, L.; Wang, W.; Zang, Z.; Chen, J. Interfacial Defect Passivation and Stress Release by Multifunctional

KPF₆ Modification for Planar Perovskite Solar Cells with Enhanced Efficiency and Stability. *Chem. Eng. J.* **2021**, *418*, 129375.

(48) Zhuang, Q. X.; Wang, H. X.; Zhang, C.; Gong, C.; Li, H. Y.; Chen, J. Z.; Zang, Z. G. Ion Diffusion-Induced Double Layer Doping toward Stable and Efficient Perovskite Solar Cells. *Nano Res.* **2022**, *15*, 5114–5122.

(49) Liu, W.; Zhang, Y. Electrical Characterization of $\text{TiO}_2/\text{CH}_3\text{NH}_3\text{PbI}_3$ Heterojunction Solar Cells. *J. Mater. Chem. A* **2014**, *2*, 10244–10249.

(50) Deng, Y.; Xu, S.; Chen, S.; Xiao, X.; Zhao, J.; Huang, J. Defect Compensation in Formamidinium–Caesium Perovskites for Highly Efficient Solar Mini-Modules with Improved Photostability. *Nat. Energy* **2021**, *6*, 633–641.

(51) Chen, M.; Kamarudin, M. A.; Baranwal, A. K.; Kapil, G.; Ripolles, T. S.; Nishimura, K.; Hirotsani, D.; Sahamir, S. R.; Zhang, Z.; Ding, C.; Sanehira, Y.; Bisquert, J.; Shen, Q.; Hayase, S. High-Efficiency Lead-Free Wide Band Gap Perovskite Solar Cells Via Guanidinium Bromide Incorporation. *ACS Appl. Energy Mater.* **2021**, *4*, 5615–5624.

(52) Aharon, S.; Dymshits, A.; Rotem, A.; Etgar, L. Temperature Dependence of Hole Conductor Free Formamidinium Lead Iodide Perovskite Based Solar Cells. *J. Mater. Chem. A* **2015**, *3*, 9171–9178.

(53) Zheng, Y.; Wu, X.; Liang, J.; Zhang, Z.; Jiang, J.; Wang, J.; Huang, Y.; Tian, C.; Wang, L.; Chen, Z.; Chen, C.-C. Downward Homogenized Crystallization for Inverted Wide-Bandgap Mixed-Halide Perovskite Solar Cells with 21% Efficiency and Suppressed Photo-Induced Halide Segregation. *Adv. Funct. Mater.* **2022**, *32*, 2200431.

(54) Bush, K. A.; Frohna, K.; Prasanna, R.; Beal, R. E.; Leijtens, T.; Swifter, S. A.; McGehee, M. D. Compositional Engineering for Efficient Wide Band Gap Perovskites with Improved Stability to Photoinduced Phase Segregation. *ACS Energy Lett.* **2018**, *3*, 428–435.

(55) Yang, Z.; Rajagopal, A.; Jo, S. B.; Chueh, C.-C.; Williams, S.; Huang, C.-C.; Katahara, J. K.; Hillhouse, H. W.; Jen, A. K. Y. Stabilized Wide Bandgap Perovskite Solar Cells by Tin Substitution. *Nano Lett.* **2016**, *16*, 7739–7747.

(56) Tucker, S. H. Lxxiv.—Iodination in the Carbazole Series. *J. Chem. Soc.* **1926**, 129, 546–553.

(57) Heller, J.; Lyman, D. J.; Hewett, W. A. The Synthesis and Polymerization Studies of Some Higher Homologues of 9-Vinylcarbazole. *Makromol. Chem.* **1964**, *73*, 48–59.

(58) Shin, Y. S.; Yoon, Y. J.; Heo, J.; Song, S.; Kim, J. W.; Park, S. Y.; Cho, H. W.; Kim, G. H.; Kim, J. Y. Functionalized PFN-X (X = Cl, Br, or I) for Balanced Charge Carriers of Highly Efficient Blue Light-Emitting Diodes. *ACS Appl. Mater. Interfaces* **2020**, *12*, 35740–35747.

(59) Giannozzi, P.; Andreussi, O.; Brumme, T.; Bunau, O.; Buongiorno Nardelli, M.; Calandra, M.; Car, R.; Cavazzoni, C.; Ceresoli, D.; Cococcioni, M.; Colonna, N.; Carnimeo, I.; Dal Corso, A.; de Gironcoli, S.; Delugas, P.; DiStasio, R. A., Jr.; Ferretti, A.; Floris, A.; Fratesi, G.; Fugallo, G.; Gebauer, R.; Gerstmann, U.; Giustino, F.; Gorni, T.; Jia, J.; Kawamura, M.; Ko, H. Y.; Kokalj, A.; Kucukbenli, E.; Lazzeri, M.; Marsili, M.; Marzari, N.; Mauri, F.; Nguyen, N. L.; Nguyen, H. V.; Otero-de-la-Roza, A.; Paulatto, L.; Ponce, S.; Rocca, D.; Sabatini, R.; Santra, B.; Schlipf, M.; Seitsonen, A. P.; Smogunov, A.; Timrov, I.; Thonhauser, T.; Umari, P.; Vast, N.; Wu, X.; Baroni, S. Advanced Capabilities for Materials Modelling with Quantum Espresso. *J. Phys.: Condens. Matter* **2017**, *29*, 465901.

(60) Neese, F. Software Update: The Orca Program System—Version 5.0. *Wiley Interdiscip. Rev.: Comput. Mol. Sci.* **2022**, *12*, No. e1606.

(61) Lu, T.; Chen, F. Multiwfn: A Multifunctional Wavefunction Analyzer. *J. Comput. Chem.* **2012**, *33*, 580–592.